Optimization of the Microstructure of Porous Composite Cathodes in Solid Oxide Fuel Cells

Siamak Farhad and Feridun Hamdullahpur
Dept. of Mechanical & Mechatronics Engineering, University of Waterloo, Waterloo, Ontario, Canada N2L 3G1

DOI 10.1002/aic.12652
Published online May 11, 2011in Wiley Online Library (wileyonlinelibrary.com).

A comprehensive micromodel to predict the electrochemical performance of porous composite LSM-YSZ cathodes in solid oxide fuel cells (SOFCs) is developed. The random packing sphere model is used to estimate the cathode microstructural properties required for the micromodel. The micromodel developed takes into account the complex interdependency among the mass transport, electron and ion transports, and the electrochemical reaction, and can be used for optimization of the microstructure of porous LSM-YSZ composite cathodes. It is shown that the electrochemical performance of these cathodes depends on the microstructural variables of the cathode porosity, thickness, particle size ratio, and size and volume fraction of LSM particles. The effect of these microstructural variables on the cathode total resistance, as the objective function to achieve the optimum microstructure for the cathode, is studied through computer simulation. The results indicated that for a LSM-YSZ cathode operated at the average temperature of 1073.15 K, bulk oxygen partial pressure of 0.21 atm, and total current density of 5000 Am^{-2}, and constrained to the minimum value of 1 μm for the size of LSM particles and 0.25 for the cathode porosity, the optimum microstructure is obtained at the particle size ratio of unity, LSM particle size of 1 μm and volume fraction of 0.413, porosity of 0.25, and thickness of 60 μm. The cathode total resistance corresponding to the cathode optimized is estimated to be 0.291 Ω cm^2. © 2011 American Institute of Chemical Engineers *AIChE J,* 58: 1248–1261, 2012
Keywords: micromodeling, porous composite cathode, optimization, electrochemical performance, solid oxide fuel cell

Introduction

A solid oxide fuel cell (SOFC) is a device to generate electrical energy from chemical energy of a fossil or renewable fuel through electrochemical reactions.[1,2] Since the electrochemical reactions take place at the active sites of the anode and cathode, as electrodes of an SOFC, the improvement of the electrochemical performance of electrodes plays an important role to improve the electrical performance of the SOFC. To improve the electrochemical performance of electrodes, in addition to the use of materials with a high catalytic activity,[3–7] the electrodes can be fabricated with a composite structure with extended active sites for electrochemical reactions.[8–10]

A composite electrode is made of three phases; electron conducting particles to transport electrons, ion conducting particles to transport oxygen ions, and pores to transport reactant gases. This is in contrast with a noncomposite electrode, which is made of two phases of electron conducting particles and pores, that the electrochemical reactions can only take place at the interface of the electrode and electrolyte. In a composite electrode, the electrochemical reactions take place throughout its body, where three phases of electron conducting particles, ion conducting particles, and pores

Correspondence concerning this article should be addressed to F. Hamdullahpur at fhamdullahpur@uwaterloo.ca.

are present. The performance of composite electrodes is strongly dependent on the microstructure of the electrode. The microstructure affects significantly the activation polarization due to the change of the active sites for electrochemical reactions, the ohmic polarization due to the change of the effective electronic and ionic resistivities, and the concentration polarization due to the change of the electrode pore size.

Some experimental studies investigated the effect of the microstructure of composite electrodes on the electrochemical performance.[11–16] These studies are limited to a small number of microstructures tested at some specific operating conditions, and cannot be used to determine the optimum microstructure. Similarly, the mathematical models developed are also limited to a small range of microstructural variables and not suitable for a comprehensive optimization. For example, Costamagna et al.[17] and Nicolella et al.[18] neglected the effect of the concentration polarization; thus, their models are limited to thin electrodes with relatively large electron and ion conducting particles sizes. Kenney and Karan[19] considered the concentration polarization in their cathode model; but neglected the Knudsen diffusion effect in oxygen transport to the cathode reaction sites. Chen et al.[16] and Kenney and Karan[19] modeled the overall oxygen reduction reaction in cathode using elementary reactions;[20,21] however, due to the lack of data for the rate of elementary reactions, the validity of the overall reaction rates obtained is limited to a narrow range of the cathode microstructural variables.

In this study, a micromodel to predict the electrochemical performance of porous composite cathodes with various microstructural characteristics is developed. The cathode considered contains lanthanum strontium manganate (LSM) with the chemical composition of $(La_{0.8}Sr_{0.2})_{0.98}MnO_3$, as the electron conductor, and yttria-stabilized zirconia (YSZ) particles with the chemical composition of $(ZrO_2)_{0.92}(Y_2O_3)_{0.08}$, as the ion conductor. This type of cathode is widely used for SOFCs and available commercially.[22,23] The micromodel developed takes into account the complex interdependency among the mass transport, electron and ion transports and the electrochemical reaction, and applied to optimize the microstructure of the cathode by a set of constraints dictated by the fabrication and operational parameters. Using this model, the effect of the microstructural variables on the minimization of the cathode total resistance, as the objective function to achieve the optimum microstructure, is investigated through computer simulation. Although we considered the total resistance as the objective function of optimization, the maximization of the power density, which is essential for portable applications of SOFCs,[24] and minimization of the exergy destruction[25,26] can be considered to optimize the cathode microstructure.

Microstructure Modeling

To predict the electrochemical performance of porous composite cathodes, a detailed micromodeling is required. The micromodeling starts with the microstructure modeling through which the cathode microstructural properties including the electrochemical active area per unit volume, average size of pores, tortuosity, and effective LSM and YSZ resistivities are estimated.

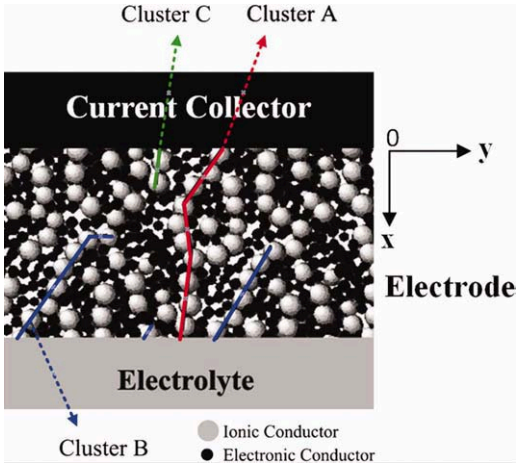

Figure 1. Schematic of a porous composite electrode.

[Color figure can be viewed in the online issue, which is available at wileyonlinelibrary.com.]

Different methods with various degrees of complexity are suggested in the literature for microstructure modeling of the porous composite electrodes.[27–38] Among them, the random packing sphere method is selected in this study due to its simplicity and low computational cost, even for small size particles. This method is applicable for the electrodes that their electron and ion conducting particles remain almost spherical during the sintering process; and loses its validity when the contact angle between particles is large. Several researcher reported that the average contact angle would be almost 30° after the sintering of SOFC's electrodes.[16,17,35,36] According to the SEM (scanning electron microscope) picture reported by Chen et al.,[16] for such an electrode the particles are almost spherical after the sintering process. Hence, for modeling the microstructure, the electrode can be assumed to be a random packing of spheres and the particle coordination number and percolation theories are used to estimate the electrode microstructural properties. Before starting the microstructure modeling using the random packing sphere method, three clusters of A, B, and C for ion and electron conducting particles are introduced. These clusters for the ion conducting particles are schematically demonstrated in Figure 1. For cluster A, the ion conducting particles are stretched from the electrolyte to the current collector. Therefore, oxygen ions can flow along the electrode and participate in the electrochemical reaction from the electrolyte to the current collector. For cluster B, the ion conducting particles are connected to the electrolyte, but not stretched to the current collector; therefore, oxygen ions can flow along the electrode and participate in the electrochemical reaction from the electrolyte to the last ion conducting particle of the chain. For cluster C, the ion conducting particles are not connected to the electrolyte and completely insulated with electron conducting particles. It is therefore impossible for oxygen ions to flow along these particles and participate in the electrochemical reactions. There is a threshold in the volume fraction of both electron and ion conducting particles under which the particles form only

clusters B and C in an electrode. The cluster A is formed above this threshold that is called the percolation threshold for cluster A. Indeed, the clusters B and C turn into cluster A and their numbers reduce when the volume fraction of the electron/ion conducting particles exceeds the percolation threshold. In this study, it is assumed that the volume fraction of both electron and ion conducting particles are beyond the percolation thresholds, thus the effect of the cluster B on the microstructural properties of the electrode is negligible.

Electrochemical active area per unit volume

To determine the electrochemical active area per unit volume of the porous composite electrode (after the sintering process), A_{TPB}, it is assumed that the electron and ion conducting particles are both mono-sized spheres distributed uniformly in the electrode. In these conditions, A_{TPB} is obtained using the statistical analysis of binary powder mixtures based on the theory of particle coordination number in the random packing of spheres and percolation theory, as Eq. 1.[17,32]

$$A_{TPB} = \left(\frac{\pi}{4}\sin^2\left(\frac{\theta_c}{2}\right)d_i^2\right)(n_t n_{el})Z_{el-io}P_{el}P_{io} \quad d_i = \min(d_{el}, d_{io}) \tag{1}$$

The number fraction of electron conducting particles, n_{el}, the total number of particles per unit volume of the electrode, n_t, and the average number of ion conducting particles in contact with an electron conducting particle, $Z_{el\text{-}io}$, are determined from Eqs. 2–4, respectively.[37]

$$n_{el} = \frac{\varphi_{el}\alpha^3}{1-\varphi_{el}+\varphi_{el}\alpha^3} \quad \left(\alpha = \frac{d_{io}}{d_{el}}\right) \tag{2}$$

$$n_t \frac{1-\varepsilon}{\frac{1}{6}\pi d_{el}^3(n_{el}+(1-n_{el})\alpha^3)} \tag{3}$$

$$Z_{el-io} = Z_{el}\frac{(1-n_{el})Z_{io}}{Z} \tag{4}$$

Bouvard and Lange[37] determined that the overall average number of contacts per particle, Z, is exactly 6 for the binary random packing of spheres. They also obtained the following equations for Z_{el}, and Z_{io}

$$Z_{el} = 3 + \frac{Z-3}{n_{el}+(1-n_{el})\alpha^2} \tag{5}$$

$$Z_{io} = 3 + \frac{(Z-3)\alpha^2}{n_{el}+(1-n_{el})\alpha^2} \tag{6}$$

In Eq. 1, the probability of cluster A of electron and ion conducting particles, P_{el} and P_{io}, are estimated from Eqs. 7 and 8, respectively.[32,39,40]

$$P_{el} = \left[1-\left(\frac{4.236-Z_{el-el}}{2.472}\right)^{2.5}\right]^{0.4} \quad (0.154<\alpha<6.464) \tag{7}$$

$$P_{io} = \left[1-\left(\frac{4.236-Z_{io-io}}{2.472}\right)^{2.5}\right]^{0.4} \quad (0.154<\alpha<6.464) \tag{8}$$

where, Z_{el-el}, and Z_{io-io}, are determined as follows[32]

$$Z_{el-el} = \frac{Zn_{el}}{n_{el}+(1-n_{el})\alpha^2} \tag{9}$$

$$Z_{io-io} = \frac{Z(1-n_{el})\alpha^2}{n_{el}+(1-n_{el})\alpha^2} \tag{10}$$

To form cluster A for both electron and ion conducting particles, the volume fraction of electron conducting particles, φ_{el}, should be limited to the percolation threshold of the electron ($P_{el}=0$) and ion ($P_{io}=0$) conducting particles. After solving Eq. 7 for $P_{el}=0$ and Eq. 8 for $P_{io}=0$, the range of the volume fraction of electron conducting particles to form cluster A is obtained

$$\frac{1}{2.4\alpha+1} < \varphi_{el} < \frac{1}{\frac{\alpha}{2.4}+1} \quad (0.154<\alpha<6.464) \tag{11}$$

Average diameter of pores and tortuosity

To estimate the average diameter of pores, d_{pores}, it is assumed that the pores are cylindrical, stretched from the current collector to the electrolyte with an average tortuosity of τ. Kenney et al.[38] showed in their computer modeling that more than 99% of the pores of an electrode are open from the current collector to the electrolyte. Therefore, all pores can be assumed to be open and the average diameter of the pores can be estimated as follows

$$4\times\frac{V_{pores}}{A_{pores}} = 4\times\frac{\frac{\pi}{4}d_{pores}^2\tau\delta N_{pores}}{\pi d_{pores}\tau\delta N_{pores}} = d_{pores} \tag{12}$$

Assuming that the surface area of the solid part of a porous electrode does not change significantly in the sintering process, the left side of Eq. 12 can be developed as follows

$$4\times\frac{V_{pores}}{A_{pores}} = 4\times\frac{V_{pores}}{V_{solid}}\times\frac{V_{solid}}{A_{pores}} \approx 4\times\frac{\varepsilon}{1-\varepsilon}\times\frac{V_{solid}}{A_{solid}}$$
$$\approx 4\times\frac{\varepsilon}{1-\varepsilon}\times\frac{\frac{\pi}{6}d_{el}^3 n_{el}+\frac{\pi}{6}d_{io}^3 n_{io}}{\pi d_{el}^2 n_{el}+\pi d_{io}^2 n_{io}} = \frac{2}{3}\left(\frac{\varepsilon}{1-\varepsilon}\right)\frac{d_{el}}{\left(\varphi_{el}+\frac{1-\varphi_{el}}{\alpha}\right)} \tag{13}$$

Therefore

$$d_{pores} \approx \frac{2}{3}\left(\frac{\varepsilon}{1-\varepsilon}\right)\frac{d_{el}}{\left(\varphi_{el}+\frac{1-\varphi_{el}}{\alpha}\right)} \tag{14}$$

The average tortuosity is estimated from the following equation

$$\varepsilon = \frac{V_{pores}}{V_{pores}+V_{solid}} = \frac{\frac{\pi}{4}d_{pores}^2\tau\delta N_{pores}}{WL\delta} \tag{15}$$

or

$$\tau = \frac{\varepsilon}{\frac{\pi}{4}d_{pores}^2\frac{N_{pores}}{WL}} \tag{16}$$

In Eq. 16, N_{pores}/WL denotes the number of pores per unit area of the porous electrode and can be estimated with the number of solid particles per unit area as follows

$$\frac{N_{pores}}{WL} \approx n_t^{2/3} \tag{17}$$

After substituting Eq. 17 into Eq. 16, the average tortuosity for a porous composite electrode is obtained as follows

$$\tau \approx \frac{\varepsilon}{\frac{\pi}{4} d_{pores}^2 n_t^{2/3}} \tag{18}$$

LSM and YSZ effective resistivities

The effective resistivity of the LSM and YSZ particles in a porous composite cathode for the particle contact angles usual for SOFCs can be estimated on the basis of the characteristics of the pure material and percolation theory, from the following eqaution[36]

$$R_i^{eff} = \frac{R_i^0}{[(1-\varepsilon)\varphi_i P_i]^{1.5}}, \quad i \in \{LSM, YSZ\} \tag{19}$$

The pure electronic resistivity of LSM with the chemical composition of $La_{0.8}Sr_{0.2}MnO_3$, and the pure ionic resistivity of YSZ with the chemical composition of $(ZrO_2)_{0.92}(Y_2O_3)_{0.08}$, as a function of temperature, can be estimated from Eqs. 20 and 21, respectively.[19]

$$R_{LSM}^0 = 5.618 \times 10^{-9} T_s \exp\left(\frac{16,600}{R_u T_s}\right) \tag{20}$$

$$R_{YSZ}^0 = 1.263 \times 10^{-9} T_s \exp\left(\frac{111,000}{R_u T_s}\right) \tag{21}$$

Micromodeling of porous LSM-YSZ cathodes

The micromodel of the composite cathode developed in this study is a steady-state one-dimensional model in the thickness direction of the cathode (x direction in Figure 1). It is assumed that the ionic conductivity of LSM and electronic conductivity of YSZ particles are negligible. The cathode layer considered is the functional layer and the effect of the current collector layer that may contain only LSM particles and pores is not taken into account.

On the basis of the Kirchhoff's circuit law, the electronic and ionic local current densities along the LSM and YSZ conductors are obtained from Eqs. 22 and 23, respectively.[17]

$$\frac{di_{LSM}(x)}{dx} = -A_{TPB} i_n(x) \quad i_{LSM}(0) = i_{tot} \tag{22}$$

$$\frac{di_{YSZ}(x)}{dx} = A_{TPB} i_n(x) \quad i_{YSZ}(0) = 0 \tag{23}$$

To solve these differential equations, the transfer current density per unit of electrochemical active area, $i_n(x)$, should be determined for the oxygen reduction reaction

$$O_2 + 4e^- \underset{k_b}{\overset{k_f}{\rightleftarrows}} 2O^{2-} \tag{R1}$$

For this purpose, the charge transfer between the electron and ion conductors is assumed to be the rate determining step of reaction R1, and the effect of the adsorption and dissociation of oxygen molecules on the electrocatalytic surface of the cathode is assumed to be negligible in this study.[17] The reaction order of unity is also assumed for this reaction in the presence of the LSM and YSZ particles.

The local rate of the forward and backward reactions can be expressed as follows

$$\vartheta_f(x) = k_f(x) C_{O_2}(x) \tag{24}$$

$$\vartheta_b(x) = k_b(x) \tag{25}$$

Where $k_f(x)$ and $k_b(x)$ denote the forward and backward reaction rates, respectively, and can be estimated from the transition state theory[41]

$$k_f(x) = A_f T_s \exp\left(\frac{-\Delta g_f(x)}{R_u T_s}\right) \tag{26}$$

$$k_b(x) = A_b T_s \exp\left(\frac{-\Delta g_b(x)}{R_u T_s}\right) \tag{27}$$

In these equations, $\Delta g_f(x)$, and $\Delta g_b(x)$ are the actual standard Gibbs function of activation for the forward and backward reactions, respectively. These two parameters can be expressed in terms of the equilibrium standard Gibbs function of activation and the energy change of electron for the cathode polarized from the equilibrium to a desired voltage[42] (the absolute value of the voltages are considered in this study)

$$k_f(x) = A_f T_s \exp\left(\frac{-\Delta g_f^\circ + 4F\beta(E_{O_2}^\circ - V(x))}{R_u T_s}\right) \tag{28}$$

$$k_b(x) = A_b T_s \exp\left(\frac{-\Delta g_b^\circ + 4F(1-\beta)(E_{O_2}^\circ - V(x))}{R_u T_s}\right) \tag{29}$$

The transfer current density per unit of electrochemical active area is then obtained from the transfer current densities of the forward and backward reactions[4]

$$\begin{aligned} i_n(x) &= 4Fk_f(x)C_{O_2}(x) - 4Fk_b(x) \\ &= 4FC_{O_2}(x)A_f T_s \exp\left(\frac{-\Delta g_f^\circ}{R_u T_s}\right)\exp\left(\frac{4F\beta(E_{O_2}^\circ - V(x))}{R_u T_s}\right) \\ &\quad - 4FA_b T_s \exp\left(\frac{-\Delta g_b^\circ}{R_u T_s}\right)\exp\left(\frac{-4F(1-\beta)(E_{O_2}^\circ - V(x))}{R_u T_s}\right) \end{aligned} \tag{30}$$

At equilibrium, $i_n(x) = 0$, $V(x) = E_{rev}$, and $C_{O_2}(x) = C_{O_2}(0)$. Therefore, the exchange current density of cathode, $i_{0,C}$, can be determined from Eq. 30 as follows

$$i_{0,C} = 4FC_{O_2}(0)A_f T_s \exp\left(\frac{-\Delta g_f^\circ}{R_u T_s}\right) \exp\left(\frac{4F\beta(E_{O_2}^\circ - E_{rev,O_2})}{R_u T_s}\right)$$
$$= 4FFA_b T_s \exp\left(\frac{-\Delta g_b^\circ}{R_u T_s}\right) \exp\left(\frac{-4F(1-\beta)(E_{O_2}^\circ - E_{rev,O_2})}{R_u T_s}\right) \quad (31)$$

After determining the cathode exchange current density, Eq. 30 can be simplified as follows

$$\frac{i_n(x)}{i_{0,C}} = \left[\frac{C_{O_2}(x)}{C_{O_2}(0)} \exp\left(\frac{4F\beta\eta_C(x)}{R_u T_s}\right) - \exp\left(\frac{-4F(1-\beta)\eta_C(x)}{R_u T_s}\right)\right] \quad (32)$$

In Eq. 32, $\eta_C(x) = E_{rev} - V(x)$ is the local cathode polarization. The reversible voltage, E_{rev}, is obtained from the Nernst relation for reaction R1

$$E_{rev,O_2} = E_{O_2}^\circ + \frac{R_u T_s}{4F} \ln \frac{C_{O_2}(0)}{C_C} \quad (33)$$

After substituting Eq. 33 into Eq. 31, the cathode exchange current density is simplified as

$$i_{0,C} = 4FA_f T_s C_C \left(\frac{C_{O_2}(0)}{C_C}\right)^{1-\beta} \exp\left(\frac{-\Delta g_f^\circ}{R_u T_s}\right) \quad (34)$$

If it is assumed that the transfer coefficient, β, is equal to 0.5[42] and air is treated as an ideal gas, ($C_{O_2} = p_{O_2}/(R_u T_s)$), Eqs. 32 and 34 can be expressed as follows

$$i_n(x) = i_{0,C}\left[\frac{p_{o_2}(x)}{p_{o_2}(0)} \exp\left(\frac{2F\eta_C(x)}{R_u T_s}\right) - \exp\left(\frac{-2F\eta_C(x)}{R_u T_s}\right)\right] \quad (35)$$

$$i_{0,C} = \frac{4FA_f p_C}{R_u} \left(\frac{p_{O_2}(0)}{p_C}\right)^{0.5} \exp\left(\frac{-\Delta g_f^\circ}{R_u T_s}\right) \quad (36)$$

Different values for the equilibrium standard Gibbs function of activation, Δg_f°, for the LSM-YSZ cathodes, ranging from 100 to 200 kJ mol^{-1}, are reported in the literature.[43] This wide range may be related to different LSM chemical compositions employed to fabricate the cathodes by various researchers. In this study, the value of 120 kJ/mol, reported by Co et al.,[43] for Δg_f°, and the value of 3×10^8 for $4FA_f p_C/R_u$ are chosen for the $(La_{0.8}Sr_{0.2})_{0.98}MnO_3$-$(ZrO_2)_{0.92}(Y_2O_3)_{0.08}$ cathode operated close to the atmospheric pressure.

According to Eqs. 35 and 36, the exchange current density is constant at a given temperature and bulk oxygen partial pressure; however, the local transfer current density is a function of the cathode local polarization, $\eta_C(x)$, and local oxygen partial pressure, $p_{O_2}(x)$. To determine the cathode local polarization, we start from Eq. 37[17]

$$\eta_C(x) = E_{rev,O_2} - V(x) = E_{rev,O_2} - (V_{YSZ}(x) - V_{LSM}(x)) \quad (37)$$

Using Ohm's law in Eqs. 38 and 39,[17] the first derivative of $\eta_C(x)$ is expressed as Eq. 40

$$\frac{dV_{LSM}(x)}{dx} = -R_{LSM}^{eff} i_{el}(x) \quad (38)$$

$$\frac{dV_{YSZ}(x)}{dx} = -R_{YSZ}^{eff} i_{io}(x) \quad (39)$$

$$\frac{d\eta_C(x)}{dx} = -\left(\frac{V_{YSZ}(x)}{dx} - \frac{V_{LSM}(x)}{dx}\right) = R_{YSZ}^{eff} i_{YSZ}(x) - R_{LSM}^{eff} i_{LSM}(x) \quad (40)$$

Using Kirchhoff's circuit law in Eqs. 22 and 23, the second derivative of $\eta_C(x)$ establishes a relation between the local cathode polarization and the local transfer current density

$$\frac{d^2\eta_C(x)}{dx^2} = R_{YSZ}^{eff} \frac{di_{YSZ}(x)}{dx} - R_{LSM}^{eff} \frac{di_{LSM}(x)}{dx} = (R_{YSZ}^{eff} + R_{LSM}^{eff}) A_{TPB} i_n(x) \quad (41)$$

To obtain the local oxygen partial pressure, the dusty gas model (DGM) is used.[44–46] The DGM includes the Stefan-Maxwell diffusion equation and takes into account the Knudsen diffusion. Using the DGM and considering that only oxygen is consumed in cathode, the following equation is obtained for the local partial pressure of oxygen

$$\frac{dp_{O_2}(x)}{dx} = -R_u T_s \left(\frac{1}{D_{K,O_2}^{eff}} + \frac{1}{D_{O_2-N_2}^{eff}}\right)\left(1 - \frac{p_{O_2}(x)}{p_C}\right) \dot{n}_{O_2}''(x) \quad (42)$$

In this equation, the effective ordinary and Knudsen diffusion coefficients are obtained from Eqs. 43[47] and 44,[48] respectively.

$$D_{O_2-N_2}^{eff} = \frac{0.0101325}{\left(V_{a,O_2}^{1/3} + V_{a,N_2}^{1/3}\right)^2} \left(\frac{1}{MW_{O_2}} + \frac{1}{MW_{N_2}}\right)^{0.5} \frac{T_s^{1.75}}{p_C} \left(\frac{\varepsilon_C}{\tau_C}\right) \quad (43)$$

$$D_{K,O_2}^{eff} = 48.5\, d_{pores} \sqrt{\frac{T_s}{MW_{O_2}}} \left(\frac{\varepsilon_C}{\tau_C}\right) \quad (44)$$

Where the atomic diffusion volume, V_a, of O_2 and N_2 is 16.3 and 18.5 cm^3, respectively.[47]

In Eq. 42, the rate of the oxygen flux in x direction, $\dot{n}_{O_2}''(x)$, is determined from the mass transfer equation as follows

$$\frac{d\dot{n}_{O_2}''(x)}{dx} = \frac{1}{4F}\frac{di_{LSM}(x)}{dx} = -\frac{A_{TPB} i_n(x)}{4F} \quad (45)$$

According to Eqs. 41, 42, and 45, the local cathode polarization and oxygen partial pressure are both function of the local transfer current density. Therefore, the system of equations 46 should be solved to determine the local transfer current density, cathode polarization, partial pressure of oxygen, and rate of oxygen flux.

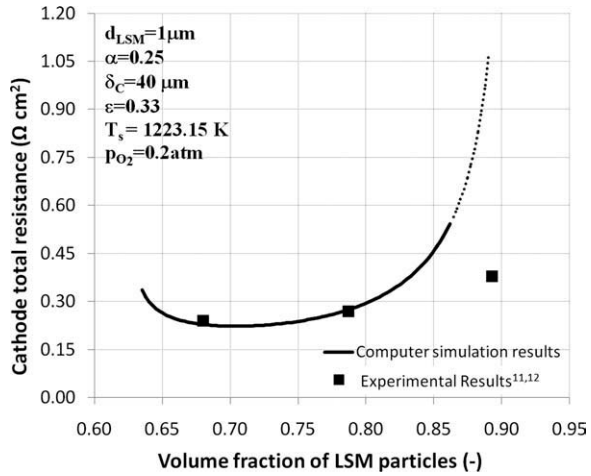

Figure 2. The results of the computer simulation and experiment for the cathode samples fabricated by Kim et al.[11,12]

$$\begin{cases} \dfrac{d^2\eta_C(x)}{dx^2} = (R^{\text{eff}}_{YSZ} + R^{\text{eff}}_{LSM}) A_{TPB} i_n(x) \\ \dfrac{dp_{O_2}(x)}{dx} = -R_u T_s \left(\dfrac{1}{D^{\text{eff}}_{k,O_2}} + \dfrac{1}{D^{\text{eff}}_{O_2-N_2}} \right) \left(1 - \dfrac{p_{O_2}(x)}{p_C} \right) \dot{n}''_{O_2} \\ \dfrac{d\dot{n}''_{O_2}}{dx} = -\dfrac{A_{TPB} i_n(x)}{4F} \\ i_n(x) = i_{0,C} \left[\dfrac{p_{O_2}(x)}{p_{O_2}(0)} \exp\left(\dfrac{4F\beta\eta_C(x)}{R_u T\ T_s} \right) \right. \\ \left. - \exp\left(\dfrac{-4F(1-\beta)\eta_C(x)}{R_u T\ T_s} \right) \right] \end{cases} \quad (46)$$

$$\text{At } x = 0 \qquad d\eta_C/dx = -R^{\text{eff}}_{LSM} i_{tot}, p_{O_2} = p_{O_2}(0), \dot{n}''_{O_2} = i_{tot}/4F$$

$$\text{At } x = \delta_c \qquad d\eta_C/dx = R^{\text{eff}}_{YSZ} i_{tot}$$

After solving the system of equations, the local current densities along the LSM and YSZ particles in x direction are determined from Eqs. 22 and 23, respectively.

The cathode total polarization and total resistance are determined from Eqs. 47 and 48, respectively.[16]

$$\eta_{C,tot} = \frac{R^{\text{eff}}_{LSM} R^{\text{eff}}_{YSZ}}{R^{\text{eff}}_{LSM} + R^{\text{eff}}_{YSZ}} \left(\frac{\eta_C(0)}{R^{\text{eff}}_{YSZ}} + i_{tot}\delta_C + \frac{\eta_C(\delta_C)}{R^{\text{eff}}_{LSM}} \right) \quad (47)$$

$$R_{C,tot} = \frac{\eta_{C,tot}}{i_{tot}} \quad (48)$$

Validation of the model

We simulated the cathode samples fabricated by Kim et al.[11,12] and Barbucci et al.[15] using a computer code developed based on our model. Kim et al.[11,12] reported valuable experimental results to correlate the cathode total resistance to the weight fraction of the YSZ particles. Their experiments were conducted for the cathode samples with the thickness of 40 μm and average LSM and YSZ particles size of 1 μm and 0.25 μm, respectively, operated at the temperature of 1223.15 K and bulk oxygen partial pressure of 0.2 atm. While they did not provide any value for the porosity and average contact angle between the LSM and YSZ particles, we used 0.33 following Smith et al.[49] and 60° from Chen et al.,[16] respectively. The computer simulation results for Kim et al.'s cathode samples are obtained and shown in Figure 2. The computer simulation could predict the total resistance of their cathode samples with the LSM volume fraction, φ_{LSM}, of 0.69 and 0.79 with the relative error of 4.6% and 2.0%, respectively. However, a significant difference is seen for the cathode with the LSM volume fraction of 0.89 that is close to the percolation threshold of the YSZ particles. Near the percolation threshold, the effect of the cluster B of YSZ particles on the cathode microstructural properties is significant. Since, we did not consider the effect of cluster B particles, our model will not be applicable near and beyond the percolation thresholds.

Barbucci et al.[15] reported some experimental results to correlate the total resistance of the porous LSM-YSZ cathode to the cathode thickness. We simulated their cathode samples ($d_{LSM} = 0.3$ μm, $d_{YSZ} = 0.3$ μm, $\varphi_{LSM} = 0.5$, $\varepsilon = 0.4$, $T_s = 1073.15$ K, $p_{O_2}(0) = 0.21$ atm) and compared to their experimental results in Figure 3. A good agreement between the computer simulation and experimental results were obtained for the cathode thickness at which the minimum cathode total resistance is obtained (≈45–50 μm). The relative error of ~15% were also obtained that may be due to the difference between the chemical composition of the LSM used to fabricate the cathodes, $(La_{0.75}Sr_{0.25})_{0.95}MnO_3$, and that used in our computer code, $(La_{0.8}Sr_{0.2})_{0.98}MnO_3$.

Results and Discussion

Cathode microstructural properties

The effect of the volume fraction of electron conducting particles, φ_{el}, at different particle size ratios, α, and sizes of the electron conducting particles, d_{el}, on the electrochemical active area per unit volume of the porous composite electrode, A_{TPB}, is shown in Figure 4. The electrochemical active

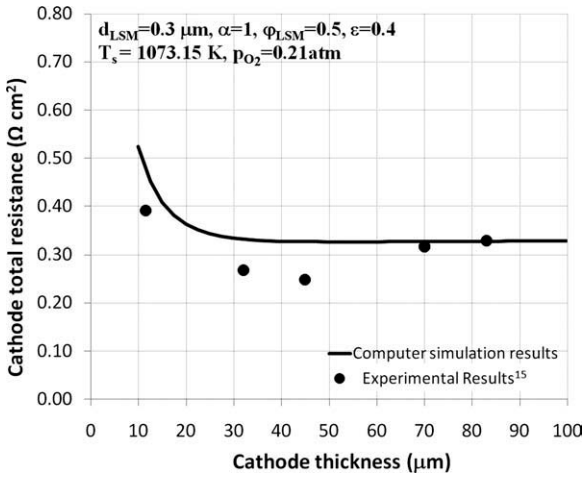

Figure 3. The results of the computer simulation and experiment for the cathode samples fabricated by Barbucci et al.[15]

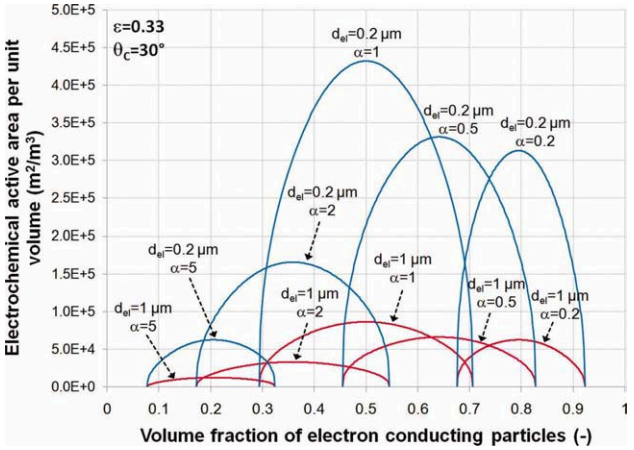

Figure 4. The effect of the volume fraction of electron conducting particles at different particle size ratios and sizes of the electron conducting particles, on the electrochemical active area per unit volume.

[Color figure can be viewed in the online issue, which is available at wileyonlinelibrary.com.]

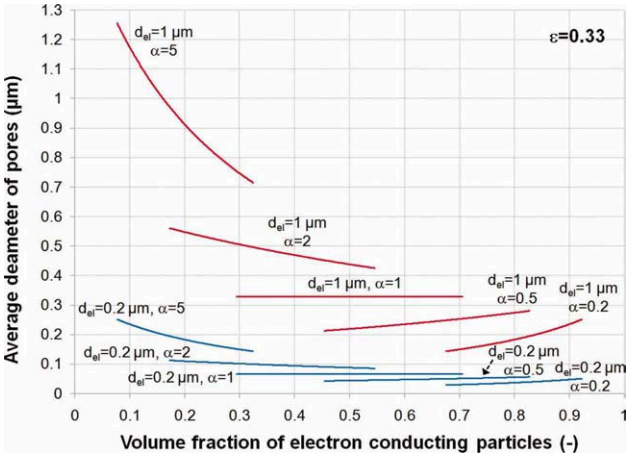

Figure 5. The effect of the volume fraction of electron conducting particles at different particle size ratios and electron conducting particle sizes on the average pore size.

[Color figure can be viewed in the online issue, which is available at wileyonlinelibrary.com.]

area per unit volume is maximized at the average volume fraction of the electron and ion conducting particles at percolation thresholds, i.e., $\varphi_{el} = (3.38\alpha + 2.4)/(2.4\alpha^2 + 6.76\alpha + 2.4)$, and increases when the particle size ratio approaches unity ($\alpha = 1$) or the size of the electron conducting particles decreases. The electrochemical active area decreases considerably at the percolation threshold of the electron or ion conducting particles; thus, it is expected that the activation polarization increases significantly at percolation thresholds. As a general results, the maximum electrochemical active area is obtained when the size and volume fraction of electron and ion conducting particles are identical.

The effect of the volume fraction of electron conducting particles at different particle size ratios and electron conducting particle sizes, on the average electrode pore size is shown in Figure 5. As seen in this figure, with an increase in the volume fraction of electron conducting particles, the pore size decreases if the value of particle size ratio is greater than unity ($\alpha > 1$), and increases if this value is smaller than unity ($\alpha < 1$). For the particle size ratio of unity ($\alpha = 1$), the average pore size remains constant throughout the entire range of the volume fraction of electron conducting particles. This result is consistent with the computer modeling result reported by Kenney et al.[38] For the particle size ratio of unity, the pore size decreases linearly with a decrease in the size of the particles. Although decreasing the size of the particles leads to an increase in the electrochemical active area of the electrode, and consequently decreasing the activation polarization, this may inhibit the gas transport from the bulk to the active sites of the electrode and increase the concentration polarization.

The effect of the LSM volume fraction at different particle size ratios and temperature of 1073.15 K on the effective electronic resistivity of LSM with the chemical composition of $La_{0.8}Sr_{0.2}MnO_3$, and ionic resistivity of YSZ with the chemical composition of $(ZrO_2)_{0.92}(Y_2O_3)_{0.08}$, is shown in Figure 6. For a given particle size ratio, the effective resistivities of LSM and YSZ are independent of the LSM particle size. A sudden jump in the effective LSM and YSZ resistivities is seen near their corresponding percolation threshold. This sudden jump is due to the assumption that the effect of cluster B particles is not taken into account in the microstructure modeling. The effective resistivity of YZS is greater than that of LSM by several orders of magnitude. The lower the YSZ resistivity, the lower the ohmic polarization; hence, the effective resistivity of YZS may play an important role to determine the optimum microstructure of the cathode. The resistivity of YSZ can decrease with a decrease in the LSM volume fraction or an increase in the particle size ratio. Since the increase of the particle size ratio or decrease of the LSM volume fraction may lead to a decrease

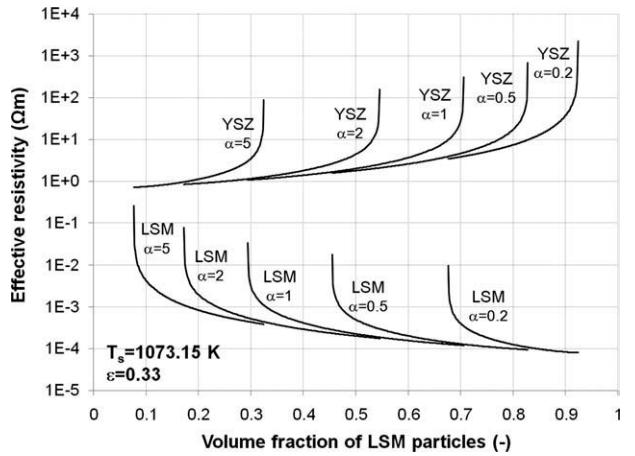

Figure 6. The effect of the LSM volume fraction at different particle size ratios on the effective LSM and YSZ resistivities (the contact angle between the percolated LSM or YSZ particles is 30°).

Table 1. The Range of the Cathode Microstructural Variables and Operating Conditions in the Optimization Process

Item	Range
Porosity	0.15–0.5
Thickness, μm	10–125
LSM particle size, μm	0.01–3.0
Particle size ratio	0.154–6.464
Volume fraction of LSM particles	$1/(2.4\alpha + 1) - 1/(\alpha/2.4 + 1)$
Temperature, K	973.15–1173.15
Bulk oxygen partial pressure, atm	0.05–0.21
Total current density, A/m^2	0–10,000

in the electrochemical active area and consequently an increase in the activation polarization, the final effect of the microstructural variables on the cathode performance should be determined through a detailed micromodeling.

Optimum microstructure of the LSM-YSZ cathode

According to the model developed, for the given cathode operating conditions, the electrochemical performance of the porous composite cathode is dependent on the microstructural variables of the porosity, thickness, particle size ratio, and LSM particle size and volume fraction. It should be noted that for a random packing of spherical particles with a given size, the porosity would be within a certain range. However, the porosity can increase if a pore former is used to fabricate the cathode or decrease if the duration or temperature of the sintering process increases through which the contact angle between particles reduces. In these conditions, the porosity will be an independent microstructural variable. The goal is to determine the value of the independent microstructural variables at which the minimum total resistance of the porous $(La_{0.8}Sr_{0.2})_{0.98}MnO_3$-$(ZrO_2)_{0.92}(Y_2O_3)_{0.08}$ composite cathode is obtained. The range of these variables and operating conditions of the cathode used for the optimization process is listed in Table 1.

The effect of the LSM volume fraction on the cathode total resistance is shown in Figure 7. As seen, with an increase in the volume fraction of LSM, the cathode total resistance decreases to a certain value and then increases. Therefore, there is an optimum LSM volume fraction at which the cathode total resistance is minimized. Our studies in the range investigated (see Table 1) confirm that there is always such an optimum LSM volume fraction that minimizes the cathode total resistance. For the particle size ratios greater than unity, this optimum volume fraction is not expected to be among the LSM volume fractions in the range of $(3.38\alpha + 2.4)/(2.4\alpha^2 + 6.76\alpha + 2.4)$ and $1/(\alpha/2.4+1)$, because as shown in Figures 4–6, with an increase in the volume fraction of LSM in this range, the electrochemical active area and pore size decrease and the effective resistivity of YSZ increases and accordingly all three activation, concentration, and ohmic polarizations increases. This would be valid for the particle size ratios less than unity if the pore size is not too small to inhibit the oxygen transport from the bulk to the active sites of the cathode.

The effect of the particle size ratio on the cathode total resistance is also shown in Figure 7. Among the optimum LSM volume fraction obtained at different particle size ratios, the one obtained at the particle size ratio of unity provides the lowest cathode total resistance. Indeed, for a cathode microstructure with the optimum LSM volume fraction, the optimum particle size ratio is equal to 1. This result can be generalized in the range of the cathode microstructural variables and operating conditions listed in Table 1.

The optimum LSM volume fraction for a cathode with the particle size ratio of unity is obtained as a function of the LSM particle size at different cathode thicknesses, porosities, temperatures, bulk oxygen partial pressures, and current densities, and shown in Figure 8. As the LSM particle size increases, the optimum LSM volume fraction increases rapidly for LSM particle sizes less than $\sim$0.2 μm, where the contribution of the concentration polarization to determine the cathode total resistance is significant, and increases linearly with a slight slope for LSM particle sizes greater than $\sim$0.5 μm, where the contribution of the activation and ohmic polarizations are more significant. In the range of the cathode microstructure investigated, the optimum LSM volume fraction increases if the cathode thickness or total current density decreases. For the LSM particle sizes greater than $\sim$0.8 μm, the lower the porosity, the higher the optimum LSM volume fraction. For the LSM particle sizes greater than $\sim$0.3 μm, the optimum LSM volume fraction decreases if the cathode temperature reduces. The bulk partial pressure of oxygen does not affect the optimum LSM volume fraction if the average size of the LSM particles is greater than $\sim$0.5 μm.

For the particle size ratio of unity, the pore size is not a function of the LSM volume fraction (see Figure 5), the minimum effective resistivity of YSZ and maximum effective resistivity of LSM are achieved at the LSM volume fraction at percolation threshold of LSM, i.e., $\varphi_{LSM} = 0.294$ (see Figure 6), and the maximum electrochemical active area occurs at the LSM volume fraction corresponding to the average percolation thresholds of the LSM and YSZ, i.e., $\varphi_{LSM} = 0.5$ (see Figure 4). Therefore, at the particle size ratio of unity, the concentration polarization does not change with

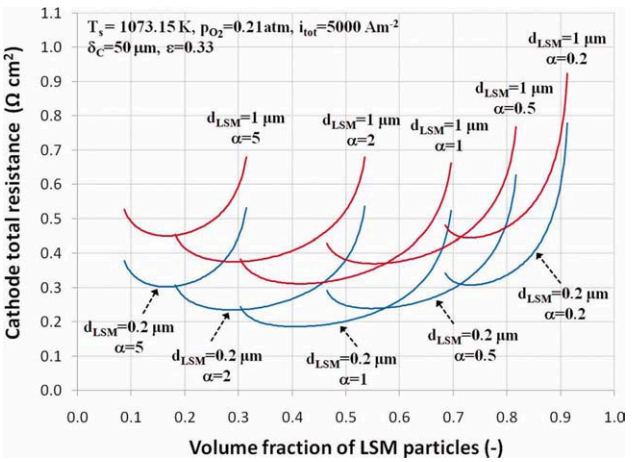

Figure 7. The effect of the LSM volume fraction at different LSM particle sizes and particle size ratios on the cathode total resistance.

[Color figure can be viewed in the online issue, which is available at wileyonlinelibrary.com.]

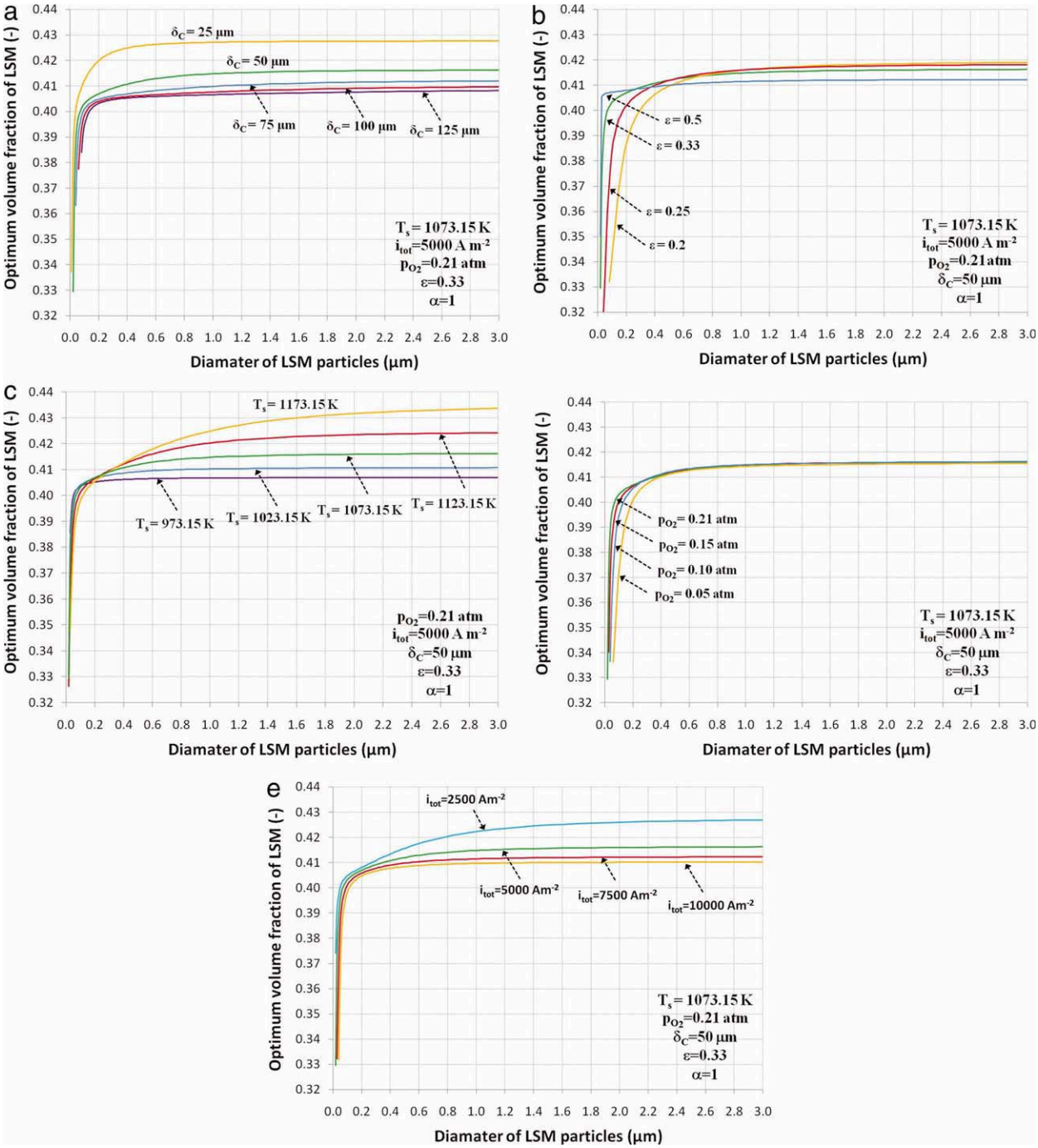

Figure 8. The effect of the LSM particle size on the optimum LSM volume fraction at different cathode (a) thicknesses, (b) porosities, (c) temperatures, (d) bulk oxygen partial pressures, and (e) current densities.

[Color figure can be viewed in the online issue, which is available at wileyonlinelibrary.com.]

the LSM volume fraction; the ohmic polarization is minimized at the LSM volume fraction of 0.294 because the effective resistivity of YSZ is much higher than that of LSM; and the activation polarization is minimized at the LSM volume fraction of 0.5. Hence, the optimum LSM volume fraction should lie between 0.294 and 0.5 for the particle size ratio of unity. This result is consistent with the results obtained from the mathematical modeling in Figure 8.

The effect of the LSM particle size on the cathode total resistance for a cathode with the optimum LSM volume fraction and particle size ratio of unity is obtained at different cathode thicknesses, porosities, temperatures, bulk oxygen partial pressures, and current densities, and shown in Figure 9. As seen in this figure, with a decrease in the LSM particle size, the cathode total resistance decreases to a certain value and then increases. Therefore, there is an optimum size for the LSM

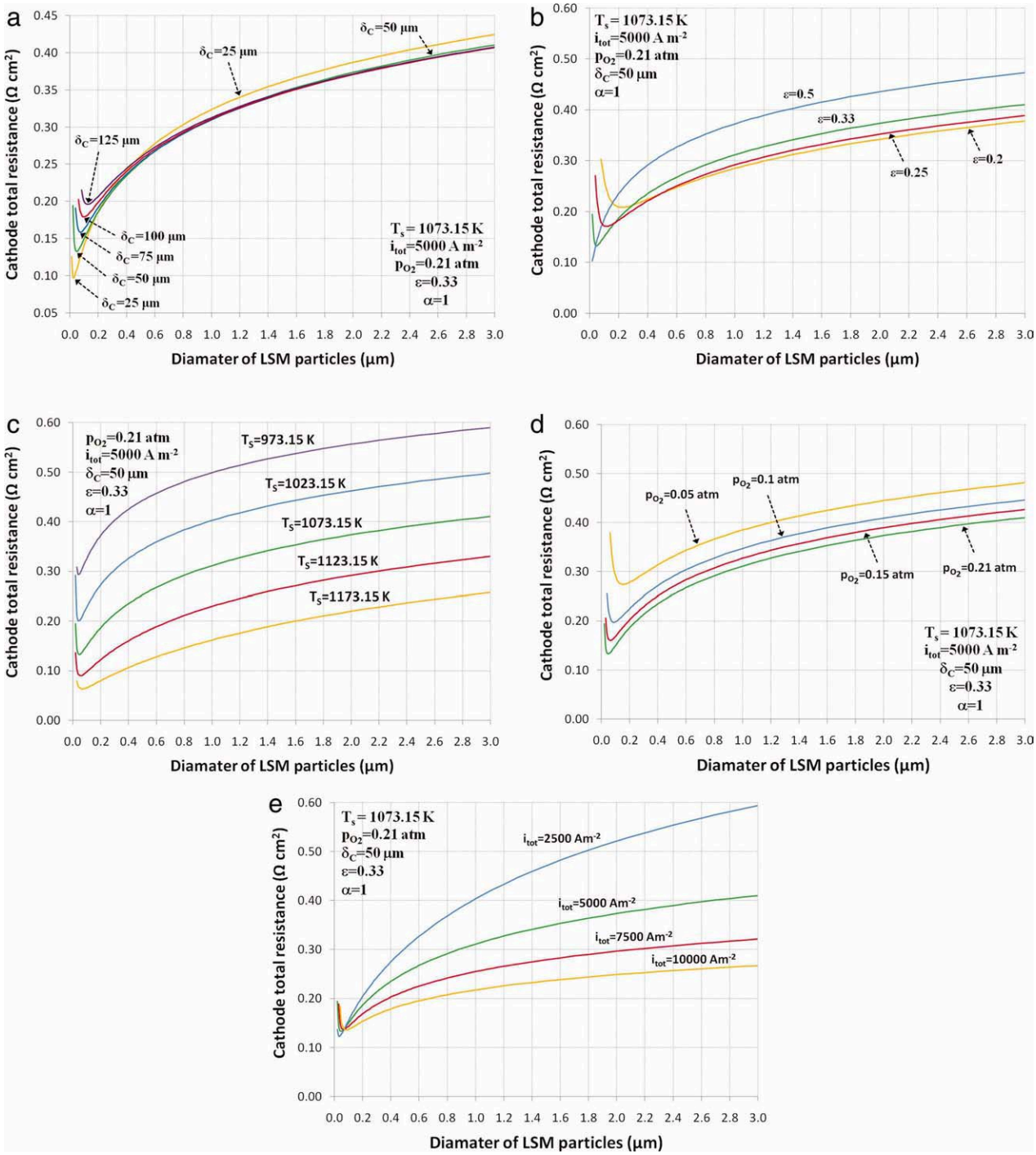

Figure 9. The effect of the LSM particle size on the cathode total resistance at different cathode (a) thicknesses, (b) porosities, (c) temperatures, (d) bulk oxygen partial pressures, and (e) current densities.

[Color figure can be viewed in the online issue, which is available at wileyonlinelibrary.com.]

particles at which the cathode total resistance is minimized. It is noted that for the particle size ratio of unity, with a decrease in the LSM particle size, the cathode activation polarization decreases due to the increase in the electrochemical active area, the cathode concentration polarization increases due to the decrease in the average pore size, and the ohmic polarization remain constant because the effective resistivity of the LSM and YSZ are not a function of the size of particles. Since the contribution of the activation polarization in the cathode total resistance is greater than that of the concentration polarization for the LSM particles larger than the optimum size, the cathode total resistance decreases with a decrease in the LSM particle size. In contrast, for the LSM particles smaller than the optimum size, the contribution of

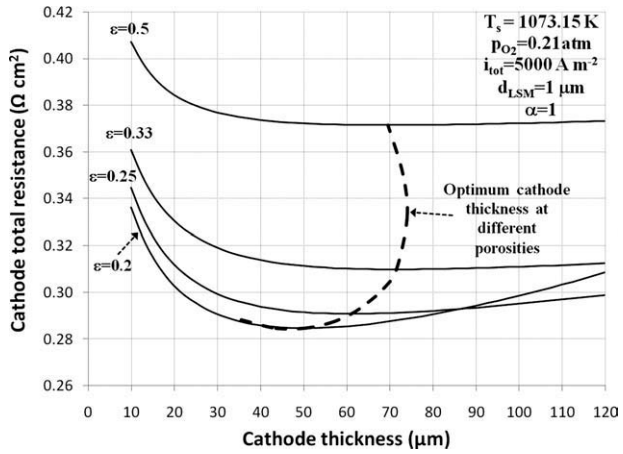

Figure 10. The effect of the cathode thickness at different porosities on the cathode total resistance.

the concentration polarization is greater than that of the activation polarization; hence, the cathode total resistance increases with a decrease in the size of the LSM particles.

As shown in Figure 9, the optimum size of the LSM particles is usually smaller than 0.2 μm. Although using the LSM particles in the range of the optimum size leads to a decrease in the total resistance, the cathode may be vulnerable to degradation due to an extensive grain growth of the particles during the sintering process or operation.[50,51] The grain growth significantly reduces the active area per unit volume and leads to an increase in the cathode total resistance. This necessitates the optimum LSM particle size to be selected by durability analysis rather than the electrochemical performance analysis presented in this article. To prevent an extensive grain growth, a minimum size of 1 μm is chosen for the LSM particles, and applied as a constraint in the optimization process.

The effect of the cathode thickness on the total resistance with the optimum LSM volume fraction, particle size ratio of unity, and the optimum size of the LSM particles constrained to a minimum value of 1 μm, is obtained at different cathode porosities and shown in Figure 10. As seen in this figure, with an increase in the cathode thickness, the total resistance decreases to a certain value and then increases linearly with a slight slope. Therefore, there is an optimum value for the cathode thickness at which the cathode total resistance is minimized. The trend that is seen from the prediction of our model is consistent with the experimental results reported by Barbucci et al.[15] This trend also makes sense physically because for thin cathodes (e.g., <10 μm) the activation polarization increases significantly due to the insufficient active sites for the electrochemical reaction R1. For thick cathodes (e.g., >100 μm), the contribution of ohmic and concentration polarizations become significant due to the increase in the mass and charge transport length.

By connecting the optimum cathode thicknesses at different cathode porosities, the dashed curve shown in Figure 10 is obtained. The minimum value of this curve, where the gradient of the cathode total resistance is zero, determines the optimum cathode porosity and thickness; and consequently, the optimum microstructure of the cathode. For a cathode operated at the average temperature of 1073.15 K, bulk oxygen partial pressure of 0.21 atm, and total current density of 5000 Am^{-2}, and with the minimum LSM particle size of 1 μm, the optimum cathode microstructure is obtained at the particle size ratio of unity, LSM volume fraction of 0.416, LSM particle size of 1 μm, thickness of 50 μm, and porosity of 0.2. The cathode total resistance corresponding to this optimum microstructure is predicted to be $\sim$0.285 Ω cm^2. If the optimum porosity of 0.2 is not achievable, the minimum possible porosity can be considered as another constraint in the optimization process.

For the optimum cathode microstructure obtained, the temperature, total current density, and bulk oxygen partial pressure were assumed to be uniform throughout the cathode. Since a distribution of these parameters is expected in the cathode, we investigated the cathode operation with the optimized microstructure at the range of the operating conditions listed in Table 1. We predicted a sudden jump in the local cathode resistance due to the limitation of the oxygen transport to the reaction active sites, at the local current density values greater than 7000 Am^{-2}, when the local temperature and bulk oxygen partial pressure are 973.15 K and 0.05 atm, respectively. To prevent such a sudden jump, a constraint for one of the microstructural variables can be considered in the optimization process. If the minimum cathode porosity of 0.25 is considered as another constraint of the optimization process, the new optimum cathode microstructure is obtained at the particle size ratio of unity, LSM volume fraction of 0.413, LSM particle size of 1 μm, cathode thickness of 60 μm, and porosity of 0.25. No sudden jump in the local cathode resistance is predicted for this new cathode microstructure in the range of the cathode local operating conditions listed in Table 1. The cathode total resistance of $\sim$0.291 Ω cm^2 is also predicted for the new optimized microstructure. It should be noted that for a random packing of spherical particles with a given size, the porosity may not be less than a certain value if the average contact angle

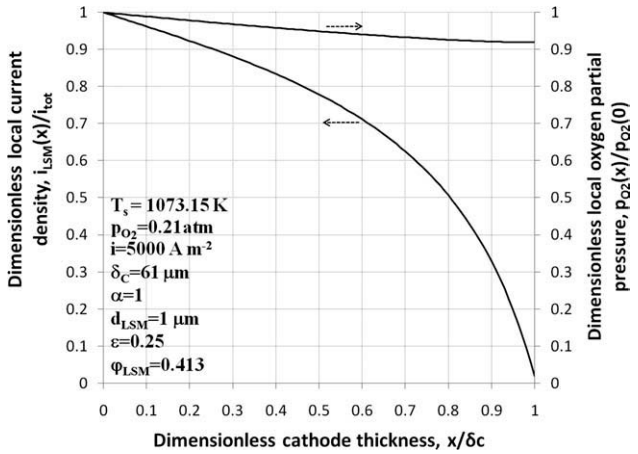

Figure 11. The distribution of the local current density and oxygen partial pressure along the thickness of the cathode with the microstructure optimized.

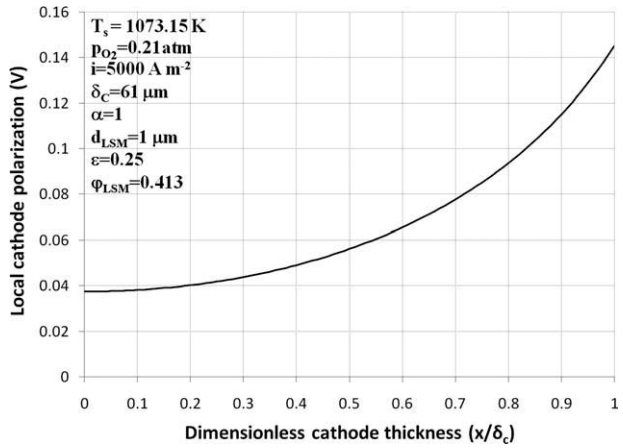

Figure 12. The distribution of the local cathode polarization along the thickness of the cathode with the microstructure optimized.

between particles is not increased in the sintering process. In such a situation, if the optimum porosity is not achievable, the minimum possible porosity for the cathode should be considered as a constraint in the optimization process.

Distribution of the current density, oxygen partial pressure, and cathode polarization

The distribution of the local current density along the thickness of the cathode with the microstructure optimized is shown in Figure 11. As seen in this figure, more than 50% of the electric current is consumed within 20% of the cathode thickness near the cathode/electrolyte interface. It means, more than 50% of the electrochemical reaction R1 takes place within 20% of the cathode near the cathode/electrolyte interface. Figure 11 also shows that only 10% of the electric current is consumed within 25% of the cathode thickness near the cathode/current collector interface.

The distribution of the local oxygen partial pressure along the thickness of the cathode with the optimized microstructure is shown in Figure 11. As seen, the local oxygen partial pressure decreases linearly with a slight slope along the cathode thickness. The oxygen partial pressure decreases only about 8% at the cathode/electrolyte interface with respect to the bulk oxygen partial pressure.

The distribution of the local cathode polarization along the thickness of the cathode with the microstructure optimized is shown in Figure 12. The local cathode polarization increases approximately as a parabolic function along the cathode thickness. The increase of the local cathode polarization is negligible at the cathode/current collector interface, and maximum at the cathode/electrolyte interface.

Conclusions

A new model to predict the electrochemical performance of the porous composite cathode was developed and applied to optimize the microstructure of the LSM-YSZ cathode by a set of constraints. The model developed indicated that the electrochemical performance of the cathode is dependent on the measurable microstructural variables of the porosity, thickness, particle size ratio, and size and volume fraction of the LSM particles. Our studies in the range of the cathode microstructural variables and operating conditions investigated confirmed that there is always an optimum LSM volume fraction at which the cathode total resistance is minimized. Among the optimum LSM volume fraction obtained at different particle size ratios, the one obtained at the particle size ratio of unity always provides the lowest total resistance. For any cathode microstructure with the optimum LSM volume fraction and particle size ratio of unity, there is an optimum LSM particle size at which the cathode total resistance is minimized. Since the optimum size of the LSM particles does not usually exceed 0.2 μm, a constraint was considered for the minimum size of the LSM particles. For any cathode microstructure with the optimum LSM volume fraction, particle size ratio of unity, and the LSM particles constrained to a minimum value of 1 μm, there is an optimum cathode thickness at which the cathode total resistance is minimized. Among the optimum cathode thicknesses obtained at different porosities, the one that provides the lowest total resistance determines the optimum microstructure.

For the porous $(La_{0.8}Sr_{0.2})_{0.98}MnO_3$-$(ZrO_2)_{0.92}(Y_2O_3)_{0.08}$ composite cathode operated at the average temperature of 1073.15 K, bulk oxygen partial pressure of 0.21 atm, and total current density of 5000 A/m^2, and constrained to the minimum value of 1 μm for the size of the LSM particles and 0.25 for the cathode porosity, the optimum cathode microstructure was obtained at the LSM volume fraction of 0.413, particle size ratio of unity, LSM particle size of 1 μm, porosity of 0.25, and thickness of 60 μm. The total resistance corresponding to this optimum cathode microstructure was predicted to be $\sim$0.291 Ω cm^2. For this optimum cathode, more than 50% of the oxygen reduction reaction takes place within 20% of the cathode thickness near the cathode/electrolyte interface, where the oxygen partial pressure reduces 8% with respect to the bulk oxygen partial pressure, and only 10% of the reaction occurs within 25% of the cathode thickness near the cathode/current collector interface.

Acknowledgments

The authors gratefully acknowledge the financial support provided by the Natural Sciences and Engineering Research Council (NSERC) of Canada.

Notation

A_{TPB} = electrochemical active area per unit volume of electrode, m^2/m^3
A = area (m^2) / coefficient of reaction rate constant, m/s K or mol/m^2. s. K
C = concentration, mol/m^3
d = diameter, m
D = diffusivity, m^2/s
E° = standard voltage, V
E_{rev} = reversible voltage, V
F = Faraday's constant, C/mol
g = molar Gibbs free energy, J/mol
i = current density, A/m^2
i_0 = exchange current density, A/m^2
i_n = transfer current density per unit of electrochemical active area, A/m^2
k = reaction rate constant, m/s or mol/m^2.s

L = length of electrode, m
M_w = molecular weight, kg/kmol
nW = number fraction of electron or ion conducting particles
$\dot{n}''_{O_2}$ = rate of oxygen flux, mol/m^2.s
N_{pores} = number of pores in an electrode
n_t = total number of particles per unit volume of electrode, 1/m^3
p = pressure, Pa
P = cluster probability of ion or electron conducting particle
R = resistivity, Ω m
$R_{C,tot}$ = cathode total resistance, Ω m^2
R_u = universal gas constant, J/mol. K
T = temperature, K
V = volume, m^3 / voltage, V
W = width of electrode, m
x = spatial coordinate along the cathode thickness
Z = overall average number of contact to a particle
Z_{el} = average number of contacts of both electron and ion conducting particles to an electron conducting particle
Z_{io} = average number of contacts of both electron and ion conducting particles to an ion conducting particle
$Z_{el—el}$ = average number of electron conducting particles in contact with an electron conducting particle
$Z_{el\text{-}io}$ = average number of ion conducting particles in contact with an electron conducting particle
$Z_{io—io}$ = average number of ion conducting particles in contact with an ion conducting particle

Greek letters

α = particle size ratio, d_{io}/d_{el}
β = transfer coefficient
δ = electrode thickness, m
ε = porosity
η = polarization, V
ϑ = rate of reaction, mol/m^2 s
φ = volume fraction of electron or ion conducting particle
θ_c = contact angle between an electron and ion conducting particle, rad
τ = tortuosity

Subscripts

b = backward reaction
C = cathode
el = electron conducting particle
f = forward reaction
io = ion conducting particle
K = Knudsen diffusion
s = solid part of an electrode
tot = total

Superscripts

0 = pure material
eff = effective

Literature Cited

1. Farhad S, Hamdullahpur F. Developing fuel map to predict the effect of fuel composition on the maximum voltage of solid oxide fuel cells. *J Power Sources*. 2009;191:407–416.
2. Farhad S, Hamdullahpur F. Developing fuel map to predict the effect of fuel composition on the maximum efficiency of solid oxide fuel cells. *J Power Sources*. 2009;193:632–638.
3. Kuhn JN, Ozkan US. Surface properties of Sr- and Co-doped $LaFeO_3$. *J Catalysis*. 2008;253:200–211.
4. Nikolla E, Schwank J, Linic S. Comparative study of the kinetics of methane steam reforming on supported Ni and Sn/Ni alloy catalysts: the impact of the formation of Ni alloy on chemistry, *J Catalysis*. 2009;263:220–227.
5. Gorte RJ, Vohs JM. Novel SOFC anodes for the direct electrochemical oxidation of hydrocarbons. *J Catalysis*. 2003;216:477–486.
6. Sfeir J, Buffat PA, Mockli P, Xanthopoulos N, Vasquez R, Mathieu HJ, herle JV, Thampi K R. Lanthanum chromite based catalysts for oxidation of methane directly on SOFC anodes. *J Catalysis*. 2001;202:229–244.
7. Adler SB, Chen XY, Wilson JR. Mechanisms and rate laws for oxygen exchange on mixed-conducting oxide surfaces. *J Catalysis*. 2007;245:91–109.
8. Haanappel VAC, Mertens J, Rutenbeck D, Tropartz C, Herzhof W, Sebold D, Tietz F. Optimisation of processing and microstructural parameters of LSM cathodes to improve the electrochemical performance of anode-supported SOFCs. *J Power Sources*. 2005;141:216–226.
9. King DL, Strohm JJ, Wang X, Roh H, Wang C, Chin Y, Wang Y, Lin Y, Rozmiarek R, Singh P. Effect of nickel microstructure on methane steam-reforming activity of Ni–YSZ cermet anode catalyst. *J Catalysis*. 2008;258:356–365.
10. Xia C, Liu M. Microstructures, conductivities, and electrochemical properties of $Ce_{0.9}Gd_{0.1}O_2$ and GDC–Ni anodes for low-temperature SOFCs. *Solid State Ionics*. 2002;152–153:423–430.
11. Kim J-D, Kim G-D, Moon J-W, Lee H-W, Lee K-T, Kim C-E. The effect of percolation on electrochemical performance. *Solid State Ionics*. 2000;133:67–77.
12. Kim J-D, Kim G-D, Moon J-W, Park Y-i, Lee W-H, Kobayashi K, Nagai M, Kim C-E. Characterization of LSM–YSZ composite electrode by ac impedance spectroscopy. *Solid State Ionics*. 2001;143:379–389.
13. Princivalle A, Djurado E. Nanostructured LSM/YSZ composite cathodes for IT-SOFC: a comprehensive microstructural study by electrostatic spray deposition. *Solid State Ionics*. 2008;179:1921–1928.
14. Liu Y, Compson C, Liu M. Nanostructured and functionally graded cathodes for intermediate temperature solid oxide fuel cells. *J Power Sources*. 2004;138:194–198.
15. Barbucci A, Carpanese MP, Viviani M, Vatistas N, Nicolella C. Morphology and electrochemical activity of SOFC composite cathodes: I. experimental analysis. *J Appl Electrochem*. 2009;39:513–521.
16. Chen XJ, Chan SH, Khor KA. Simulation of a composite cathode in solid oxide fuel cells. *Electrochim Acta*. 2004;49:1851–1861.
17. Costamagna P, Costa P, Antonucci V. Micro-modelling of solid oxide fuel cell electrodes. *Electrochim Acta*. 1998;43:375–394.
18. Nicolella C, Bertei A, Viviani M, Barbucci A. Morphology and electrochemical activity of SOFC composite cathodes: II. Mathematical modelling. *J Appl Electrochem*. 2009;39:503–511.
19. Kenney B, Karan K. Engineering of microstructure and design of a planar porous composite SOFC cathode: a numerical analysis. *Solid State Ionics*. 2007;178:297–306.
20. Younessi-Sinaki M, Matida EA, Hamdullahpur F. Kinetic model of homogeneous thermal decomposition of methane and ethane. *Int J Hydrogen Energy*. 2009;34:3710–3716.
21. Younessi-Sinaki M, Matida EA, Hamdullahpur F. Development of a reaction mechanism for predicting hydrogen production from homogeneous decomposition of methane. *Int J Hydrogen Energy*. 2011;36:2936-2944.
22. Farhad S, Yoo Y, Hamdullahpur F. Effects of fuel processing methods on industrial scale biogas-fuelled solid oxide fuel cell system for operating in wastewater treatment plants. *J Power Sources*. 2010;195:1446–1453.
23. Farhad S, Hamdullahpur F, Yoo Y. Performance evaluation of different configurations of biogas-fuelled SOFC micro-CHP systems for residential applications. *Int J Hydrogen Energy*. 2010;35: 3758–3768.
24. Farhad S, Hamdullahpur F. Conceptual design of a novel ammonia–fuelled portable solid oxide fuel cell system. *J Power Sources*. 2010;195:3084–3090.
25. Farhad S, Saffar-Avval M, Younessi-Sinaki M. Efficient design of feedwater heaters network in steam power plants using pinch technology and exergy analysis. *Int J Energy Res*. 2007;32:1–11.
26. Farhad S, Younessi-Sinaki M, Golriz MR, Hamdullahpur F. Exergy analysis and performance evaluation of CNG to LNG converting process. *Int J Exergy*. 2008;5:164–176.
27. Sunde S. Monte Carlo simulations of polarization resistance of composite electrodes for solid oxide fuel cells. *J Electrochem Soc*. 1996;143:1930–1939.
28. Sunde S. Monte Carlo simulations of conductivity of composite electrodes for solid oxide fuel cells. *J Electrochem Soc*. 1996;143:1123–1132.
29. Ji Y, Yuan K, Chung JN. Monte-Carlo simulation and performance optimization for the cathode microstructure in a solid oxide fuel cell. *J Power Sources*. 2007;165:774–785.

30. Sunde S. Calculations of impedance of composite anodes for solid oxide fuel cells. *Electrochim Acta*. 1997;42:2637–2648.
31. Sunde S. Simulations of composite electrodes in fuel cells. *J Electroceram*. 2000;5:153.182.
32. Chan SH, Xia ZT. Anode micro-model of solid oxide fuel cell. *J Electrochem Soc*. 2001;148:A388–A394.
33. Chan SH, Chen XJ, Khor KA. Cathode micromodel of solid oxide fuel cell. *J Electrochem Soc*. 2004;151:A164–A174.
34. Kuo CH, Gupta PK. Rigidity and conductivity percolation thresholds in particulate composites. *Acta Metall Mater*. 1995;43:397–403.
35. Jeon DH, Nam JH, Charn-Jung K. Microstructural optimization of anode-supported solid oxide fuel cells by a comprehensive microscale model. *J Electrochem Soc*. 2006;153:A406–A417.
36. Nam JH, Jeon DH. A comprehensive micro-scale model for transport and reaction in intermediate temperature solid oxide fuel cells. *Electrochim Acta*. 2006;51:3446–3460.
37. Bouvard D, Lange FF. Relation between percolation and particle coordination in binary powder mixtures. *Acta Metal Mater*. 1991;39:3083–3090.
38. Kenney B, Valdmanis M, Baker C, Pharoah JG, Karan K. Computation of TPB length, surface area and pore size from numerical reconstruction of composite solid oxide fuel cell electrodes. *J Power Sources*. 2009;189:1051–1059.
39. Suzuki M, Oshima T. Estimation of the co-ordination number in a two-component mixture of cohesive spheres. *Powder Technol*. 1983;36:181–188.
40. Suzuki M, Oshima T. Estimation of the co-ordination number in a multi-component mixture of spheres. *Powder Technol*. 1983;35:166–159.
41. Li X. *Principles of Fuel Cells*. New York: Taylor & Francis, 2006.
42. Bard AJ, Faulkner LR. *Electrochemical Methods: Fundamentals and Applications*, 2nd ed. Wiley, New York, 2001.
43. Co AC, Xia SJ, Birss VI. A kinetic study of the oxygen reduction reaction at LaSrMnO3 -YSZ composite, *Electrochem Soc*. 2005;152:A570–A576.
44. Mason EA. *Gas Transport in Porous Media: the Dusty-Gas Model*. Elsevier, New York, 1983.
45. Hussain MM, Li X, Dincer I. Mathematical modeling of transport phenomena in porous SOFC anodes. *Int J Therm Sci*. 2007;46:48–56.
46. Suwanwarangkul R, Croiset E, Fowler MW, Douglas PL, Entchev E, Douglas MA. Performance comparison of Fick's, dusty-gas and Stefan–Maxwell models to predict the concentration overpotential of a SOFC anode. *J Power Sources*. 2003;122:9–18.
47. Fuller EN, Ensley K, Giddings JC. Diffusion of halogenated hydrocarbons in helium. The effect of structure on collision cross sections. *J Phys Chem*. 1969;78:3679–3685.
48. Chan SH, Khor KA, Xia ZT. A complete polarization model of a solid oxide fuel cell and its sensitivity to the change of cell component thickness. *J Power Sources*. 2001;93:130–140.
49. Smith JR, Chen A, Gostovic D, Hickey D, Kundinger D, Duncan KL, DeHoff RT, Jones KS, Wachsman ED. Evaluation of the relationship between cathode microstructure and electrochemical behavior for SOFCs. *Solid State Ionics*. 2009;180:90–98.
50. Song HS, Lee S, Hyun SH, Kim J, Moon J. Compositional influence of LSM-YSZ composite cathodes on improved performance and durability of solid oxide fuel cells. *J Power Sources*. 2009;187:25–31.
51. Song HS, Kim WH, Hyun SH, Moon J, Kimb J, Lee H-W. Effect of starting particulate materials on microstructure and cathodic performance of nanoporous LSM–YSZ composite cathodes. *J Power Sources*. 2007;167:258–264.

Manuscript received Jan. 16, 2011, and revision received Mar. 29, 2011.